Layer-independent ferromagnetic insulators in a new structural phase of Cr_2S_3

Ping Li [1,*] Chengyang Xu [2] and Weidong Luo [2,3,†]

[1]*Key Laboratory of Advanced Electronic Materials and Devices, School of Mathematics and Physics, Anhui Jianzhu University, Hefei 230601, China*

[2]*Key Laboratory of Artificial Structures and Quantum Control, School of Physics and Astronomy, Shanghai Jiao Tong University, Shanghai 200240, China*

[3]*Institute of Natural Sciences, Shanghai Jiao Tong University, Shanghai 200240, China*

(Received 12 October 2021; revised 24 January 2022; accepted 12 May 2022; published 26 May 2022)

Ferromagnetic insulators (FMIs) are crucial for sensing and storage, but they are currently rare. The magnetism of the widely studied CrI_3 and $Cr_2Ge_2Te_6$ is layer dependent; thus, obtaining FMIs from these materials is challenging because the film thickness must be carefully controlled. Based on the generalized gradient approximation (GGA), GGA + U, and HSE06 hybrid functional calculations, this work predicts a new structural phase of Cr_2S_3 (γ-Cr_2S_3) and further predicts it as an intrinsic and layer-independent FMI. The material is dynamically metastable. It crystallizes a rhombohedral lattice, stacking the Cr_2S_3 quintuple layers (QLs) along the [111] direction through van der Waals interactions. The in-plane lattice constant is 3.4 Å, and each Cr atom carries a magnetic moment of $3.0\mu_B$. γ-Cr_2S_3 behaves as an intrinsic FMI, irrespective of the layer number, but its indirect energy gap can be tuned from 1.23 to 1.97 eV by changing the film thickness according to the HSE06 calculations. In-plane compressive strain facilitates the ferromagnetism and decreases the energy gap, while tensile strain leads to antiferromagnetism and decreases the energy gap. In the 1QL case, 0.5% in-plane tensile strain causes the ferromagnetic-antiferromagnetic phase transition. The origin of the ferromagnetism and the strain-induced magnetic transition of γ-Cr_2S_3 are discussed and attributed to the dominant ferromagnetic part of the superexchange.

DOI: 10.1103/PhysRevMaterials.6.054006

I. INTRODUCTION

Ferromagnetic insulators (FMIs), which combine the advantages of ferromagnetism and insulators, are crucial for sensing, storage and topological quantum materials [1–8]. Among them, van der Waals (vdW) FMIs are of special interest because they can be mechanically exfoliated into multilayers or epitaxially grown layer by layer without many imperfections [1,2,9]. However, intrinsic FMIs are rare. Ferromagnetic (FM) crystals are usually metallic while antiferromagnetic (AFM) crystals are usually insulating. In the two-dimensional (2D) case, long-range FM order is strongly suppressed by thermal fluctuations according to the Mermin-Wagner theorem [10].

Recent experiments [1,2] have reported long-range insulating ferromagnetism in atomically thin layers of CrI_3 and $Cr_2Cr_2Te_6$. The magnetism of them is layer dependent. According to magneto-optic Kerr effect (MOKE) measurement [2], the CrI_3 monolayer is an Ising FMI with a Curie temperature (T_C) of 45 K. The ferromagnetism in the CrI_3 bilayer is suppressed while that in the CrI_3 trilayer is restored. In contrast to CrI_3, the $Cr_2Cr_2Te_6$ bilayer is a Heisenberg FMI with $T_c = 30$ K, while the FM order is not present in the monolayer limit, at least down to 4.7 K [1]. The strong layer-dependent magnetism renders the obtaining of 2D FMIs of CrI_3 and $Cr_2Cr_2Te_6$ challenging. The layer thickness must be precisely controlled though it is not easy, whether through mechanical exfoliation or layer-by-layer epitaxial synthesis. Finding vdW crystals with intrinsic and layer-independent ferromagnetism is essential and interesting, in both theory and experiment.

Here we predict a new structural phase of Cr_2S_3 (γ-Cr_2S_3) and present it as a robust intrinsic FMI. The generalized gradient approximation (GGA), GGA + U, and HSE06 hybrid functional calculations have been performed, and all the calculations lead to qualitatively consistent results. γ-Cr_2S_3, a vdW layered and dynamically metastable rhombohedral crystal, exhibits layer-independent ferromagnetism. Its energy gap can be tuned from 1.23 eV in the bulk to 1.97 eV in the monolayer limit, while its magnetic phase can be manipulated by strain. An in-plane tensile strain around 0.5% triggers the FM-to-AFM phase transition.

II. METHOD

First-principles calculations were performed within the GGA [11], GGA + U ($U = 3$ eV), and HSE06 hybrid functional [12,13] frameworks, respectively, as implemented in the VASP codes [14]. All calculations lead to qualitatively consistent results, indicating the reliability of the results. For the GGA and GGA + U calculations, the energy cutoff was 500 eV, and $16 \times 16 \times 1$ and $16 \times 16 \times 6$ Monkhorst-Pack K meshes were used for the γ-Cr_2S_3 slabs and bulks, respectively. In the HSE06 hybrid functional calculations, the hybrid mixing parameter was fixed at 0.25 as suggested in the VASP codes. The energy cutoff was 400 eV, and $12 \times 12 \times 1$ and $6 \times 6 \times 6$ K meshes were used for the slabs and bulks, respectively. A vacuum of 20 Å was introduced to all the slabs

*liping@ahjzu.edu.cn
†wdluo@sjtu.edu.cn

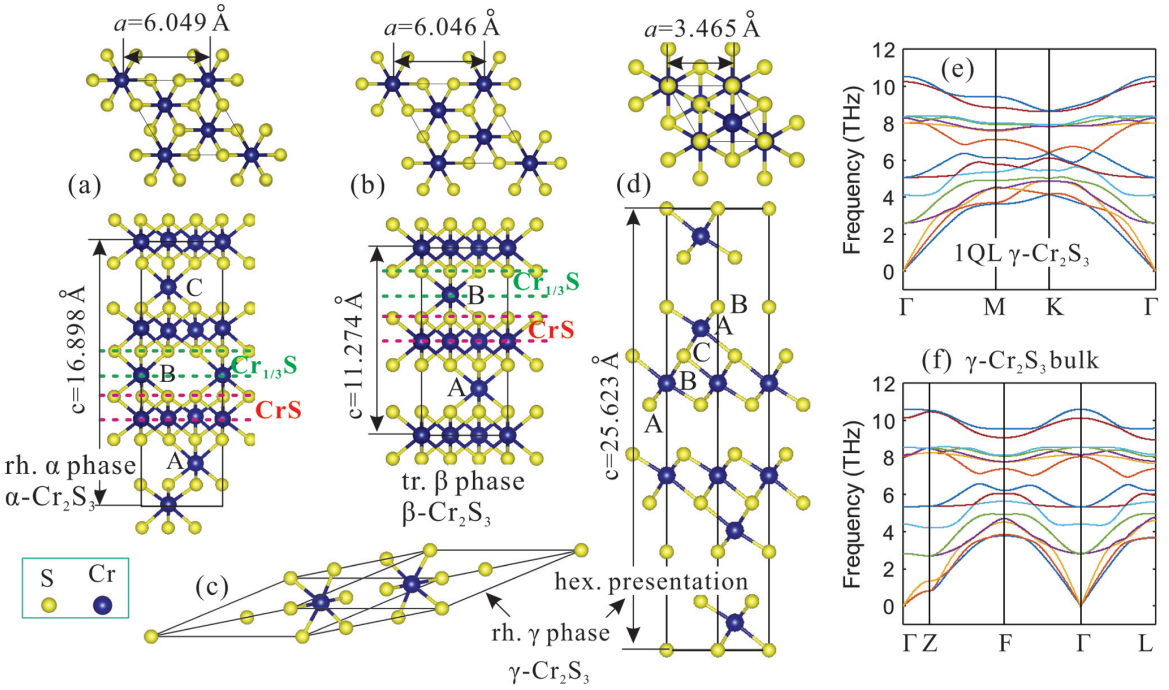

FIG. 1. Two existing structures of Cr_2S_3 in (a) rhombohedral phase and (b) trigonal phase. (c) The new rhombohedral phase of Cr_2S_3 predicted in this work and (d) its hexagonal presentation. In (a), (b), and (d), top and bottom panels correspond to top and side views, respectively. The lattice constants are obtained from GGA + U (U = 3.0 eV) calculations with vdW corrections. A, B, and C indicate the stacking sequence of atoms along the c direction. For clarity, the three structures are called α, β, and γ phases, and the corresponding materials are referred to as α-, β-, and γ-Cr_2S_3, respectively. Phonon spectra of (e) one quintuple layer (1QL) and (f) bulk γ-Cr_2S_3 calculated using the DFPT method.

to minimize the image-image interactions due to the periodic boundary condition.

The vdW correction of the optB88-vdW scheme [15] was used to correct the interlayer vdW interactions in γ-Cr_2S_3. This scheme was successfully tested on the Bi_2Se_3-family topological insulators, which have the same crystal structure as γ-Cr_2S_3. Taking Bi_2Se_3 as an example, using the optB88-vdW scheme the calculated lattice constants are $a = 4.164$ Å and $c = 28.803$ Å. If not considering the vdW correction, the obtained lattice constants are $a = 4.192$ Å and $c = 30.689$ Å. The experimental lattice parameters of Bi_2Se_3 are $a = 4.136$ Å and $c = 28.615$ Å [16]. Obviously, when the optB88-vdW correction is included, the calculated lattice constants are more satisfactory and much closer to the experimental ones. Hence, this correction was involved in all our calculations. Crystal structures were fully optimized until the force acting on each ion was less than 0.01 eV/Å. Phonon spectra were calculated using both the density functional perturbation theory (DFPT) method [17] and the finite displacement method [18] as implemented in the PHONOPY package [19] with the help of the VASP codes. The two methods gave rise to very consistent phonon dispersions; thus only the results of the DFPT method were illustrated in this work.

III. RESULTS AND DISCUSSION

A. Crystal structures of Cr_2S_3

Cr_2S_3 is known to exist in two crystallographic forms [20], a rhombohedral form and a trigonal form, with space groups of R-3 (No. 148) and P-31c (No. 163), respectively. We show their atomic geometries in Figs. 1(a) and 1(b), and briefly call them α and β phases, respectively. Both structures are constructed by a stacking of alternating CrS and Cr-deficient $Cr_{1/3}S$ layers along the c direction. The stacking manner of the CrS layers is the same, while that of the $Cr_{1/3}S$ layers differs. The Cr atoms in the $Cr_{1/3}S$ layers of α-Cr_2S_3 are stacked in the $\cdots$A-B-C-A-B-C$\cdots$ sequence, while those of β-Cr_2S_3 are stacked in the $\cdots$A-B-A-B$\cdots$ order. According to the neutron diffraction measurement [21,22], the two crystals exhibit different magnetic behaviors. α-Cr_2S_3 has three magnetic sublattices [21]. The slightly different thermal variation of the sublattice magnetization makes it act as a ferrimagnet with a Curie temperature of 122 K. β-Cr_2S_3 possesses a screw-type spiral AFM structure from 4.2 to 78 K, while it becomes paramagnetic above 125 K [22].

The predicted and investigated crystal structures of Cr_2S_3 in this work are shown in Figs. 1(c) and 1(d). It also crystallizes a rhombohedral form with space group of R-3m (No. 166) but is obviously different from the α phase in Fig. 1(a). For clarity and also to distinguish it from the two existing Cr_2S_3 crystal forms, the new rhombohedral structure is called the γ phase, and the crystal will be referred to as γ-Cr_2S_3. In this new structure, Cr and S atoms are alternately stacked in the $\cdots$A-B-C-A-B-C$\cdots$ sequence along the c direction of the hexagonal cell or the [111] direction of the rhombohedral cell, forming vdW Cr_2S_3 quintuple layers (QLs). For more information about the crystal structure of γ-Cr_2S_3, Table I lists the Wyckoff positions.

According to the GGA results, γ-Cr_2S_3 is about 0.142 and 0.141 eV/Cr higher in energy than α- and β-Cr_2S_3, respec-

TABLE I. Wyckoff positions of γ-Cr_2S_3. The crystal crystallizes a rhombohedral lattice with space group of R-3m (No. 166). The coordinates x, y, and z are obtained within the GGA + U (U = 3.0 eV) framework, with respect to the lattice constants a = 3.465 Å and c = 25.623 Å.

	Wyckoff letter	x	y	z
Cr	6c	0.0000	0.0000	0.3945
S1	3a	0.0000	0.0000	0.0000
S2	6c	0.0000	0.0000	0.2227

tively, while in the GGA + U (U = 3.0 eV) framework, the energy differences increase to 0.175 and 0.172 eV/Cr, respectively. Though about the higher energy, γ-Cr_2S_3 exhibits no imaginary phonons, both in one-QL (1QL) and bulk cases, as Figs. 1(e) and 1(f) show. Therefore, γ-Cr_2S_3 is dynamically metastable. Such a material could sometimes be realized through proper substrate or nonequilibrium techniques such as quenching.

In the following sections, we will show that γ-Cr_2S_3 is an intrinsic and layer-independent FMI. Its energy gap and magnetism can be manipulated by strains, and the mechanism of magnetism can be understood in the framework of a single-particle picture.

B. Electronic structure and magnetism of 1QL γ-Cr_2S_3

We start our discussions from 1QL γ-Cr_2S_3. To ensure the reliability of this study, first-principles calculations were performed within GGA, GGA + U, and HSE06 hybrid functional frameworks, respectively, and all these calculations lead to qualitatively consistent results.

Table II lists the GGA, GGA + U, and HSE06 hybrid functional lattice constants of 1QL γ-Cr_2S_3. These constants agree well with each other. They are all around 3.4 Å, approximately half of the lattice constants of CrI_3 and $Cr_2Ge_2Te_6$ monolayers, which are about 7 Å [23,24]. Recently, an atom-atom distance of 3.4 Å was reported on the (001) cleavage surface of α-Cr_2S_3 according to the annular dark-field aberration-corrected scanning transmission electron microscopy image [25], in very good agreement with the current data. However, it should be noted that the in-plane lattice constants of α- and β-Cr_2S_3 are much larger, about 5.9 Å [21,22].

The calculated band structure and projected density of states (PDOS) of 1QL γ-Cr_2S_3 are shown in Fig. 2, where the FM state is used. Obviously, 1QL γ-Cr_2S_3 is an indirect-gap insulator, just as CrI_3 [23,26] and $Cr_2Ge_2Te_6$ [24] monolayers are. In the GGA case, the valence band maximum (VBM) is located between the Γ and M points in the Brillouin zone, and the conduction band minimum (CBM) occurs at the M point. In GGA + U and HSE06 cases, the VBM shifts to the Γ point, but the CBM does not move. The VBM is mainly contributed by Cr t_{2g} and S p states, while the CBM is dominated by Cr e_g and S p states. The energy gaps are very different within the three calculation schemes. The GGA and GGA + U calculations generate energy gaps of 0.42 and 0.91 eV, respectively, while the HSE06 calculation gives rise to a much larger energy gap of 1.97 eV. The HSE06 energy gap of 1QL γ-Cr_2S_3 is much larger than the gaps of CrI_3 and $Cr_2Ge_2Te_6$ monolayers. Previous first-principles calculations have reported energy gaps of the CrI_3 monolayer ranging from 0.36 to 1.28 eV [23,26,27], while that of the $Cr_2Ge_2Te_6$ monolayer is about 0.91 eV [24].

To explore the magnetic ground state of 1QL γ-Cr_2S_3, four different magnetic structures are considered. They are sketched in Figs. 3(a)–3(d) and are referred to as FM, A-, C-, and G-type AFM orders, respectively. GGA, GGA + U, and HSE06 hybrid functional calculations all agree that FM phase is energetically the lowest, while the A-type AFM phase is energetically the second lowest. The energy differences ΔE between the FM and A-type AFM phases are listed in Table II, which are −6.0, −1.8, and −0.5 meV/Cr in GGA, GGA + U, and HSE06 cases, respectively, strongly suggesting the FM ground state. Each Cr atom in 1QL γ-Cr_2S_3 carries a magnetic moment of 3.0μ_B, equal to the Cr moment in $Cr_2Ge_2Te_6$ [24] and CrI_3 family materials [23]. A recent study has predicted the ferromagnetism in a different structure of 1QL Cr_2S_3 according to GGA + U calculations with U = 2.6 eV [28]. Using the same Hubbard U we successfully reproduced their results. However, we found that when the Hubbard U decreases to 1.2 eV or smaller, or within GGA and HSE06 frameworks, that slab becomes AFM because of the lower energy.

From the above discussions, 1QL γ-Cr_2S_3 is an intrinsic FMI. To gain deeper understanding of the ferromagnetism, first-principles energy of different magnetic orders in Figs. 3(a)–3(d) is fitted to the Heisenberg model:

$$H = -J_1 \sum_{\langle i,j \rangle} \vec{S}_i \cdot \vec{S}_j - J_2 \sum_{\langle\langle i,j \rangle\rangle} \vec{S}_i \cdot \vec{S}_j - J_3 \sum_{\langle\langle\langle i,j \rangle\rangle\rangle} \vec{S}_i \cdot \vec{S}_j - J_z \sum_{\langle i,j \rangle} S_{iz} S_{jz}. \quad (1)$$

Here S_i is the spin magnetic moment of a Cr atom at site i, and J_1, J_2, and J_3 correspond to the exchange coupling param-

TABLE II. Calculated lattice constants a and c, energy gaps E_g, and energy difference ΔE of 1QL and bulk γ-Cr_2S_3. Here, ΔE is the energy difference between FM order and A-type AFM order shown in Fig. 3; thus, a negative value means a FM ground state.

		a (Å)	c (Å)	E_g (eV)	ΔE (meV/Cr)
1QL γ-Cr_2S_3	GGA	3.426		0.42	−6.0
	GGA + U	3.488		0.91	−1.8
	HSE06	3.439		1.97	−0.5
Bulk γ-Cr_2S_3	GGA	3.406	25.453	−0.26	−7.3
	GGA + U	3.465	25.623	0.14	−11.4
	HSE06	3.474	26.132	1.23	−4.9

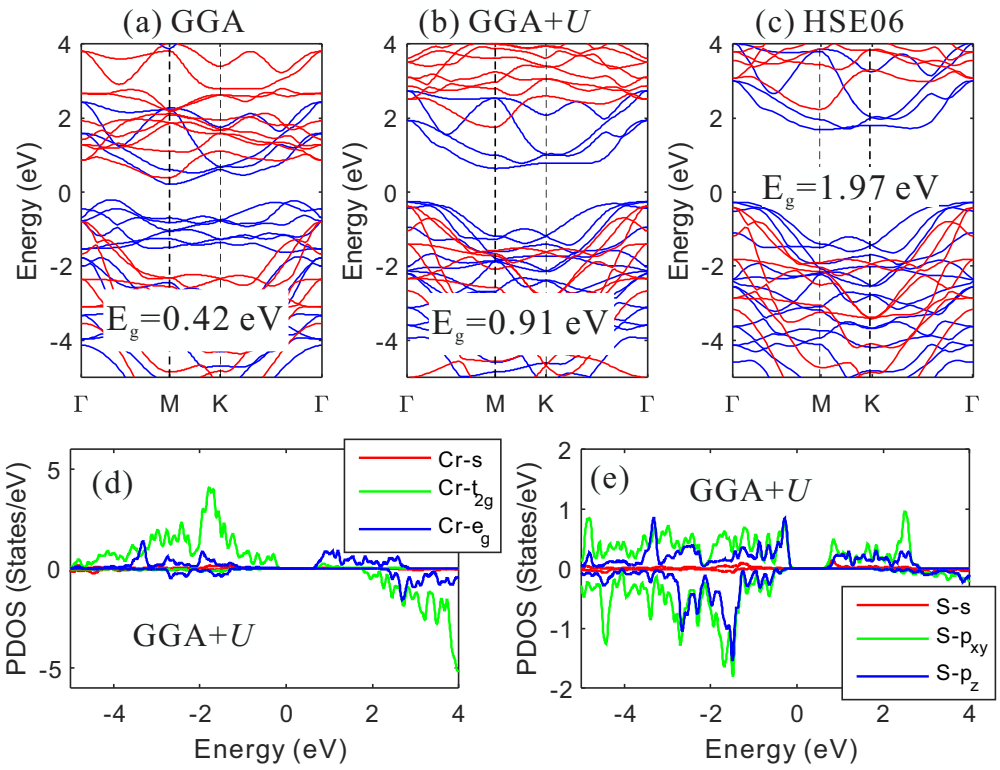

FIG. 2. Calculated band structures of FM 1QL γ-Cr_2S_3 within (a) GGA, (b) GGA + U, and (c) HSE06 hybrid functional frameworks. Blue and red lines indicate the majority- and minority-spin bands, respectively. Density of states projected on (d) Cr and (e) S atoms of 1QL γ-Cr_2S_3 within the GGA + U framework.

eters between the first-, second-, and third-nearest-neighbor (NN) Cr atoms, respectively, as sketched in Fig. 3(e). The anisotropic term is expressed as the anisotropic exchange coupling term J_z. The contribution of single-ion anisotropy is neglected due to the quenched orbital moment in Cr^{3+}. And only the anisotropic exchange between intraplane NN Cr atoms is included. Within the GGA + U framework, the obtained fit parameters are $J_1 = 2.538$ meV, $J_2 = 0.325$ meV, and $J_3 = -0.110$ meV. The first- and second-NN Cr atoms prefer FM coupling, while the third-NN Cr atoms prefer AFM coupling. The former dominates, resulting in a FM ground state.

C. Manipulating the magnetism and energy gap of 1QL γ-Cr_2S_3 through strain

Magnetism [29,30] and energy gap [8,31] can usually be tuned by strain. In this work, the in-plane strain ϵ is defined as

$$\epsilon = 100 \times \frac{(a - a_0)}{a_0}\%, \tag{2}$$

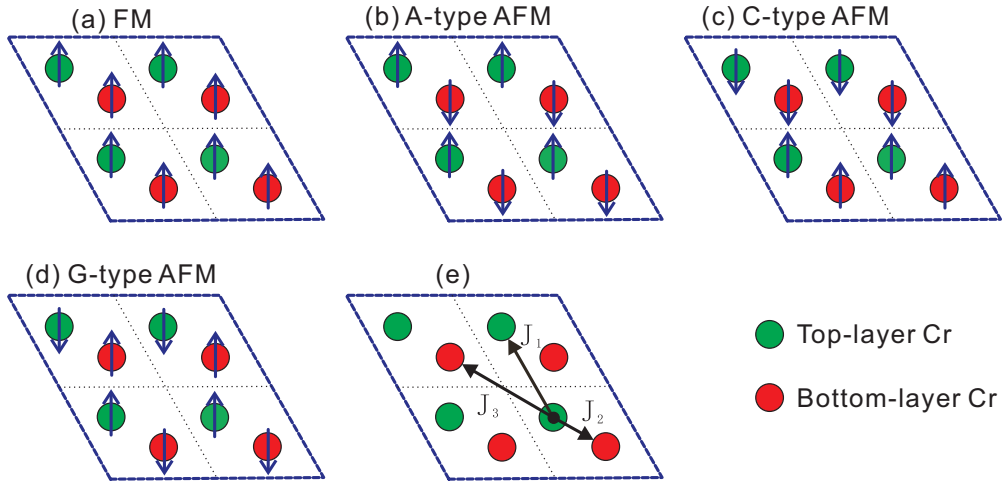

FIG. 3. [(a)–(d)] Considered magnetic orders and (e) the exchange coupling parameters of 1QL γ-Cr_2S_3. Red and green symbols denote Cr atoms of different heights, and arrows in (a) through (d) indicate the magnetization direction.

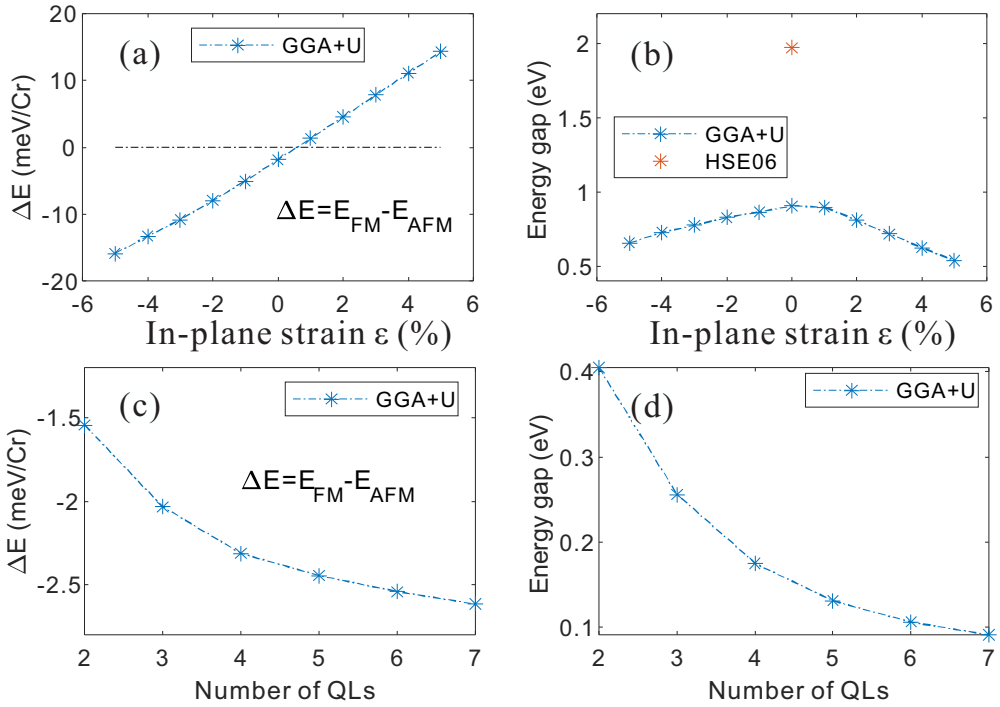

FIG. 4. (a) Energy difference ΔE and (b) band gaps of 1QL γ-Cr_2S_3 at different in-plane strain. (c) Energy difference ΔE and (d) band gaps of γ-Cr_2S_3 slabs containing different QLs.

where a and a_0 are the strained and equilibrium lattice constants, respectively. According to Eq. (2), negative and positive ϵ values correspond to compressive and tensile strains, respectively.

Figures 4(a) and 4(b) show the energy difference ΔE and the energy gap of 1QL γ-Cr_2S_3 at different in-plane strains, respectively. ΔE linearly changes following ϵ. Compressive strain facilitates the FM order, just as the $Cr_2Ge_2Te_6$ monolayer [24] behaves. Tuning ϵ from 0 to -5%, ΔE is lowered from -1.8 to -15.9 meV/Cr according to the GGA + U results (see Table III). Conversely, tensile strain harms the FM order. At about $\epsilon = 0.5\%$ ΔE becomes zero. After that ΔE becomes positive if further increasing ϵ, indicating the AFM order obtains the lower energy compared with the FM order. Therefore, $\epsilon = 0.5\%$ is the FM-AFM phase transition strain. Explicitly, the magnetic transition occurred when the interplane coupling, i.e., the total effect of J_2 and J_3, is reverted. As shown in Fig. 5(a), intraplane coupling J_1 keeps FM while the sign of $J_2 + J_3$ turns to be reverted at the transition point at $\epsilon = 0.5\%$. This strain is small; thus, the strain-induced magnetic phase transition could be easily achieved in experiment. The energy gap of 1QL γ-Cr_2S_3 varies obviously under strain. Both the compressive and tensile strains decrease the energy gap. A quite similar trend also occurs in the $Cr_2Ge_2Te_6$ monolayer [24].

D. Properties of 1QL γ-Cr_2Se_3

The properties of 1QL γ-Cr_2Se_3 are also investigated. According to GGA + U results, its in-plane lattice constant is 3.672 Å. This is larger than that of 1QL γ-Cr_2S_3, consistent with the atomic size of S and Se elements.

Though 1QL γ-Cr_2S_3 is an intrinsic FMI, 1QL γ-Cr_2Se_3 is not. Within the GGA + U framework, 1QL γ-Cr_2Se_3 is 6.1 meV/Cr lower in the AFM state than in FM order, indicating an AFM ground state. The AFM slab possesses an indirect energy gap of 0.72 eV, thus acting as an AFM insulator. However, it can be turned into a FMI by applied strains. Under in-plane compressive strains, the energy difference ΔE of 1QL γ-Cr_2Se_3 between the FM and the AFM states decreases, indicating that the slab evolves from AFM order to FM order. At $\epsilon = -2\%$, ΔE becomes negative, about -3.4 meV/Cr (see Table III). The FM order is now energetically more favorable. It obtains an indirect energy gap of 0.08 eV,

TABLE III. Cr-S(Se)-Cr angle of second-NN Cr atoms with different strain in units of degrees. ΔE is the energy difference between FM order and A-type AFM order in units of meV/Cr.

	Strain	−5%	−4%	−3%	−2%	−1%	0%	1%	2%	3%	4%	5%
1QL γ-Cr_2S_3	Cr-S-Cr	97.67	96.91	96.25	95.51	94.83	94.08	93.38	92.69	91.99	91.31	90.64
	ΔE	−15.9	−13.3	−10.8	−8.0	−5.0	−1.8	1.3	4.6	7.8	11.1	14.3
1QL γ-Cr_2Se_3	Cr-Se-Cr	97.74	96.97	96.00	95.26	94.49	93.76	92.97	92.27	91.58	90.89	90.25
	ΔE	−19.2	−13.5	−7.2	−3.4	1.2	6.1	10.6	15.7	21.0	25.4	29.7

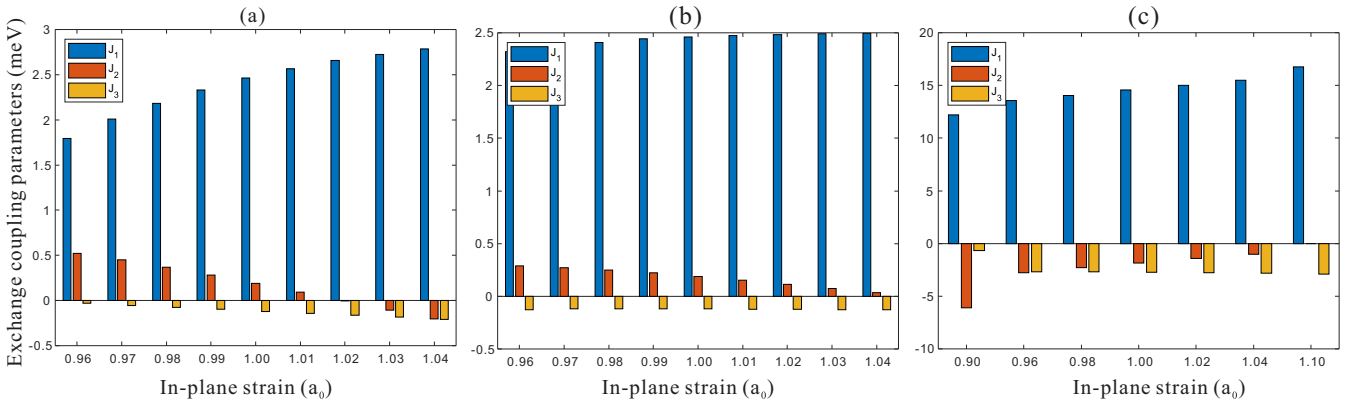

FIG. 5. Exchange coupling parameters of 1QL γ-Cr_2S_3 under in-plane strains. Atomic positions used in (a) were fully relaxed, while the fractional coordinates in (b) were fixed at those of the unstrained structure. (c) Structures are constructed with regular (CrS_6) octahedrons. The results located at point "1" in (c) denote the octahedrons with 2.55 Å Cr-S bond length. The parameters are fitted from the GGA + U ($U = 3.0$ eV) energies.

corresponding to a FMI. On the other hand, 1QL γ-Cr_2S_3 prefers out-of-plane magnetic anisotropy when compression is applied. According to previous work [32], the anisotropic exchange depends on the distortion of (CrI_6) units. Such a mechanism is inferred to work in the Cr_2S/Se_3 system because they share the same electron configuration and exchange type. Yet, the anisotropic exchange is not the main point of this article. Meanwhile, it is smaller than the interlayer magnetic coupling by one order of the magnitude. Hence, we will not include it in the following discussion about strain-tuned magnetic transition.

E. Mechanism of magnetism in 1QL γ-Cr_2S_3 and γ-Cr_2Se_3

Within common types of exchange, double exchange [33] and Ruderman-Kittel-Kasuya-Yosida exchange [34] are generally mediated by itinerant electrons. Thus, the two such types of exchange are excluded in the semiconducting γ-Cr_2S/Se_3. The magnetic coupling mainly originates from the direct exchange (DE) or superexchange (SE). In 1QL γ-Cr_2L_3 (L = S, Se), the interlayer NN Cr-Cr distance ($l_{\text{Cr-Cr}}$) is nearly 1.4 times the NN Cr-L distance ($l_{\text{Cr-}L}$). Thus it seems anomalous that the interlayer magnetism favors AFM coupling under tensile strain because the DE generally decreases more quickly than the SE. For a better understanding of such special magnetism in 1QL γ-Cr_2L_3, two questions are proposed. One is how strain induces magnetic transition. The other is why the magnetic ground state of 1QL γ-Cr_2Se_3 differs from 1QL γ-Cr_2S_3. Through analysis of the contributions from different SE paths, the two questions will be answered within the framework of the single-particle picture.

The strain-tuned intraplane NN coupling (J_1) is excluded in the discussion because it remains FM regardless of tension or compression, as shown in Fig. 5. Such trivial magnetic coupling corresponds to the well-known 90° Goodenough-Kanamori-Anderson (GKA) rule [35]. Thus, we focus on the coupling between two monatomic layers. The interplane coupling depends on the total effect of J_2 and J_3, which consist of DE and SE. Yet, the DE involved in J_2 or J_3 is not responsible for the magnetic transition. For J_3, the distance of the interlayer next-nearest-neighbor (NNN) Cr atoms reaches up to nearly 5 Å, which is too far for the DE to play a role. For J_2, the major contribution to the magnetic transition of the fully relaxed structures is determined as follows.

Table IV lists the $l_{\text{Cr-S}}$ and the $l_{\text{Cr-Cr}}$ distances in the strained 1QL γ-Cr_2S_3 in three different cases: (i) all the atoms are fully relaxed, (ii) the atoms are not relaxed but fixed at their respective fractional coordinates in the equilibrium lattice constants, and (iii) each Cr atom and its six NN S atoms keep forming a regular octagon. In case (iii), the NN and NNN Cr

TABLE IV. The Cr-S1 distances $l_{\text{Cr-S}}$ and the NN interlayer Cr-Cr distances $l_{\text{Cr-Cr}}$ in strained 1QL γ-Cr_2S_3 in three different cases: (i) both the lattice constants and the atoms are fully relaxed; (ii) when the lattice constants are strained the fractional coordinates of atoms are kept to the unstrained values; and (iii) when the strain is applied, each Cr atom and its six surrounding S atoms form a regular octagon. Here, S1 denotes a middle-layer S atom of the γ-Cr_2S_3 QL, and the distances are in units of Å.

	Strain	−4%	−3%	−2%	−1%	0%	1%	2%	3%	4%
(i)	$l_{\text{Cr-S}}$	2.524	2.534	2.542	2.552	2.559	2.568	2.577	2.586	2.595
	$l_{\text{Cr-Cr}}$	3.778	3.774	3.764	3.757	3.746	3.737	3.729	3.720	3.711
(ii)	$l_{\text{Cr-S}}$	2.457	2.482	2.508	2.533	2.559	2.585	2.610	2.636	2.661
	$l_{\text{Cr-Cr}}$	3.596	3.633	3.671	3.708	3.746	3.783	3.821	3.858	3.895
	Strain	−10%	−4%	−2%	0%	2%	4%	10%		
(iii)	$l_{\text{Cr-S}}$	2.464	2.510	2.530	2.550	2.570	2.590	2.650		
	$l_{\text{Cr-Cr}}$	3.485	3.550	3.578	3.606	3.635	3.663	3.748		

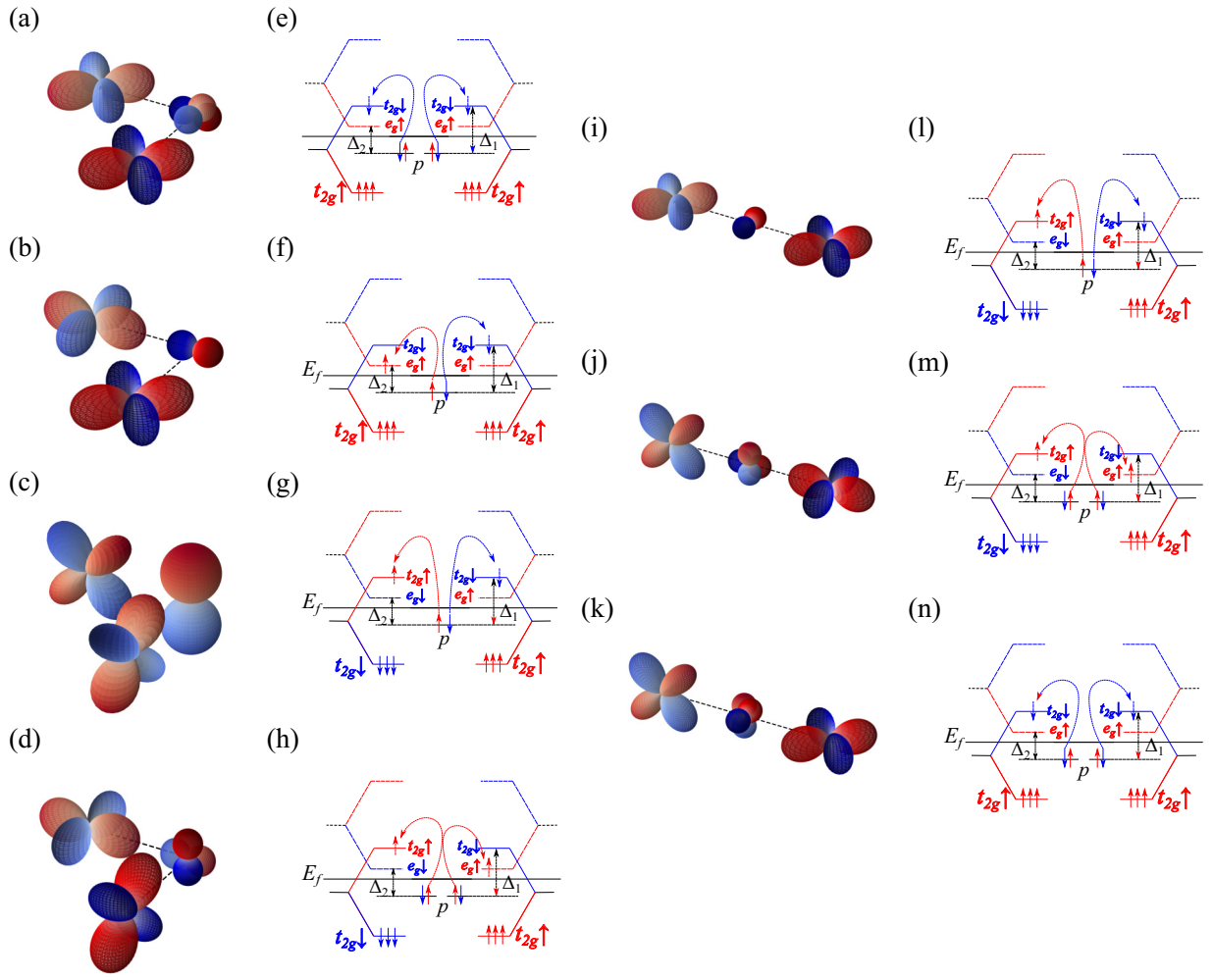

FIG. 6. The schematic figures of the paths contributing to the interlayer magnetic coupling. Δ_1 and Δ_2 are two types of energy difference. Energy levels of the d orbitals with spin up and spin down are denoted with red and blue lines. The p orbitals right below the Fermi level are denoted by black lines. The solid (dashed) arrows denote the electrons before (after) virtual hopping. The virtual hopping process is labeled by curved arrows. [(a)–(h)] The paths included in the 90° NN coupling (J_2). The local coordinates are defined with the x, y axis along two perpendicular Cr-S(Se) bonds in the Cr-S(Se)-Cr plane. [(i)–(n)] The paths included in the 180° NNN coupling (J_3).

atoms bridged by ligands form 90° and 180° angles; thus, the hopping consisting of orthogonal overlaps can be eliminated. Generally, the little deviation of the fully relaxed structures from the "perfect" structure will not cause new terms that dominate the magnetic coupling. Hence, the Cr^{3+}-Cr^{3+} direct exchange is zero due to the orthogonality of the orbitals unless the AFM t_{2g}-t_{2g} hopping is included. As the compression increases, $l_{\text{Cr-Cr}}$ gets larger in case (i) while it becomes smaller in cases (ii) and (iii). If the DE governs the change of interlayer coupling, J_2 in Fig. 5(b) will tend to be AFM since the magnitude of the DE is scaled by $l_{\text{Cr-Cr}}$. Yet, the strain-dependent J_2 in Fig. 5(b) shares a similar property but varies more moderately. It implies that the SE determines the enhanced FM (AFM) coupling when compression (tension) is applied while the AFM DE just accelerates the efficiency of reaching the critical point through strain. On the other hand, Fig. 5(c) shows, as the strain varies from negative to positive values, J_2 decreases or becomes less negative. It turns to be FM at $\epsilon = 10\%$, corresponding to $l_{\text{Cr-Cr}} = 3.748$ Å in Table IV. As mentioned at the beginning of this section, the AFM DE decays more rapidly than SE when the systems are enlarged. Thus, the FM SE bridged by 2.650 Å Cr-S bonds offsets the AFM DE spacing about 3.748 Å at the critical point. When it comes to the J_2 parameter of the relaxed structures in case (i), the $l_{\text{Cr-}L}$ distance increases from 2.524 to 2.595 Å as the strain increases from −4% to 4%. On the contrary, $l_{\text{Cr-Cr}}$ decreases from 3.778 to 3.711 Å. Based on the Cr-Cr and Cr-S atomic spacing when J_2 turns to be FM in Fig. 5(c), it can be concluded that the SE governs J_2 of the fully relaxed structures, especially the compressed ones in Fig. 5(a). Hence, it can be inferred that the SE is the key to the magnetic transition.

Then, it is essential to identify the paths dominating the magnetism and quantify their magnitudes as J_2 and J_3 are the cumulative effects from various superexchange paths. Beyond the conventional paths in GKA rules, two (one) more paths involving the empty e_g orbitals with majority spin are additionally taken into account for J_2 (J_3) as shown in Fig. 6.

The paths including energetically high-lying e_g orbitals with minority spin are neglected because the large charge-transfer energy causes the nearly negligible energy correction to the ground state.

To achieve the contribution of different paths, the Cr-L-Cr angles between the two edge or corner-shared regular octahedrons are supposed to be exactly 90° or 180°. Then, the interlayer magnetic couplings J_2 and J_3 up to the lowest order of the energy correction are given by [36]

$$\begin{aligned} J_2 \propto & -8\left(\frac{t_\pi^2}{\Delta_1}\right)^2 \frac{1}{2\Delta_1} + 16\left(\frac{t_\pi^2}{\Delta_1}\right)^2 \frac{J_H}{(2\Delta_1)^2} \\ & + 16\frac{t_\pi^2}{\Delta_1}\frac{t_\sigma^2}{\Delta_2}\frac{J_H}{(\Delta_1+\Delta_2)^2}, \\ J_3 \propto & -8\left(\frac{t_\pi^2}{\Delta_1}\right)^2 \frac{1}{2\Delta_1} - 8\frac{t_\pi^2}{\Delta_1}\frac{t_\sigma^2}{\Delta_2}\frac{J_H}{(\Delta_1+\Delta_2)^2} \\ & + 4\left(\frac{t_\pi^2}{\Delta_1}\right)^2 \frac{J_H}{(2\Delta_1)^2}, \end{aligned} \tag{3}$$

where J_H, t_π, and t_σ denote Hund's coupling, and hopping integrals through d-p_π and d-p_σ bonds. And Δ_1 (Δ_2) is the energy cost of charge transfer in the spin-down (spin-up) channel as shown in Fig. 6. For simplicity, the same J_H is adopted for intra-atom Hund exchange of Cr and ligands [36]. Here, the positive sign in Eq. (3) means the FM coupling. Details of the components of J_2 and J_3 can be found in Fig. 6 and Eq. (A1) in the Appendix.

After the tensile strain is applied, the d-p hopping integrals, t_π and t_σ, and the octahedral crystal-field splitting will experience the power-law decay with the increasing Cr-S(Se) bond length [37–40]. The hopping parts are all biquadratic in Eq. (3), and the three terms exhibit different dependence on the charge-transfer energy Δ_1 and Δ_2. Within J_2, the AFM term is proportional to $\frac{1}{\Delta_1^3}$ while the second term is proportional to $\frac{1}{\Delta_1^4}$. Relative to the p orbitals, the $3d$ orbitals evolve as schematically shown in Fig. 10. Correspondingly, Δ_1 increases and Δ_2 decreases by the magnitude of changed crystal-field splitting. Then, it is inferred that the FM term drops faster than the AFM term. Only the first two terms are included because the decreased Δ_2 partly compensates the Δ_1 induced decay of the third term. In other words, the second term will dominate the change of the FM part in the 90° J_2. Hence, the FM part of J_2 is more sensitive to the applied strain, and so is the FM part of J_3.

Now we turn to the questions presented at the beginning of this section. As discussed above, the FM coupling characterized by $\frac{1}{\Delta_1^4}$ in both J_2 and J_3 governs the response of the interlayer coupling to the strain. Thus the FM part of the interlayer coupling decreases more rapidly than the AFM term, resulting in the transition from the FM ground state to the AFM one. The second question about the different magnetic ground states of Cr_2S_3 and Cr_2Se_3 can be answered in the sense of deviation from the Cr_2S_3 without strain. In Table III, the smaller Cr-L-Cr angle implies the Cr_2Se_3 crystal structure is equivalent to the Cr_2S_3 under tension. Based on the discussion above, the AFM part tends to surpass the FM part such that the equivalently stretched Cr_2Se_3 prefers to be AFM compared to Cr_2S_3. That is why the ground states of Cr_2S_3 and Cr_2Se_3 are different at the interlayer coupling.

F. Thicker γ-Cr_2S_3 slabs

The magnetism of thicker γ-Cr_2S_3 slabs is also investigated. 2QL γ-Cr_2S_3 consists of four Cr monolayers. From bottom to top layers, the Cr atoms may magnetize along different directions, thus forming magnetic orders such as (↑↑↑↑), (↑↑↓↓), (↑↓↑↓), and (↑↓↓↑). Here ↑ and ↓ arrows mean up and down spins, respectively. According to calculations, the FM order (↑↑↑↑) is about 1.5–5.0 meV/Cr lower in energy than the other three AFM ones, indicating a FM ground state. 2QL γ-Cr_2S_3 is also an indirect-gap FMI. However, the gap is reduced to 0.41 eV from 0.91 eV in the 1QL case according to GGA + U calculations.

Figures 4(c) and 4(d) show the energy difference ΔE between the FM and AFM phases and the energy gaps of γ-Cr_2S_3 slabs from 2QLs to 7QLs, respectively. The FM state is always energetically preferable. The thicker the slab, the smaller the energy gap. It strongly indicates that the semiconducting ferromagnetism of γ-Cr_2S_3 is robust against film thickness. This is very different from CrI_3 and $Cr_2Ge_2Te_6$, where the magnetism is layere dependent. MOKE measurement [2] indicates that the CrI_3 monolayer is an Ising FMI with $T_C = 45$ K. The ferromagnetism in the CrI_3 bilayer is suppressed while that in the trilayer is restored. The $Cr_2Cr_2Te_6$ bilayer is a Heisenberg FMI with $T_c = 30$ K, while the FM order is not present in the monolayer limit down to 4.7 K [1]. The layer-independent ferromagnetism of γ-Cr_2S_3 makes it a promising compound to obtain FMIs. Using γ-Cr_2S_3 as FMIs, the precise control of the film thickness or the layer number becomes not so important or essential, though it is still useful to manipulate the gap size.

G. γ-Cr_2S_3 bulk

Stacking an infinite number of γ-Cr_2S_3 QLs along the [111] direction, γ-Cr_2S_3 bulk is achieved. According to our calculations, the bulk is also an intrinsic FMI.

The calculated lattice constants, the energy difference between the FM and AFM phases, and the energy gaps of γ-Cr_2S_3 bulk are listed in Table II, and the band structures are illustrated in Fig. 7. Within the GGA framework, the lattice constants are $a = 3.406$ Å and $c = 25.453$ Å. They can be compared with the data of CrI_3 bulk [23], where $a = 7.006$ Å and $c = 22.350$ Å. Just as the 1QL case, GGA, GGA + U, and HSE06 hybrid functional calculations lead to qualitatively consistent results. γ-Cr_2S_3 bulk energetically prefers the FM order. Each Cr atom carries a magnetic moment of $3.0\mu_B$, equal to the Cr moment in $Cr_2Ge_2Te_6$ [24] and CrI_3 family materials [23]. Though γ-Cr_2S_3 is metallic in the GGA framework, it is gapped in the other two frameworks. Considering the band-gap underestimation problem of GGA and GGA + U, HSE06 results could be more reliable [41]. Therefore, γ-Cr_2S_3 bulk is a FMI with an indirect energy gap of 1.23 eV, equal to the energy gap (1.2 eV) of CrI_3 bulk [23].

Three calculation schemes give rise to similar PDOS, and the GGA + U and HSE06 results are illustrated in Fig. 8. The

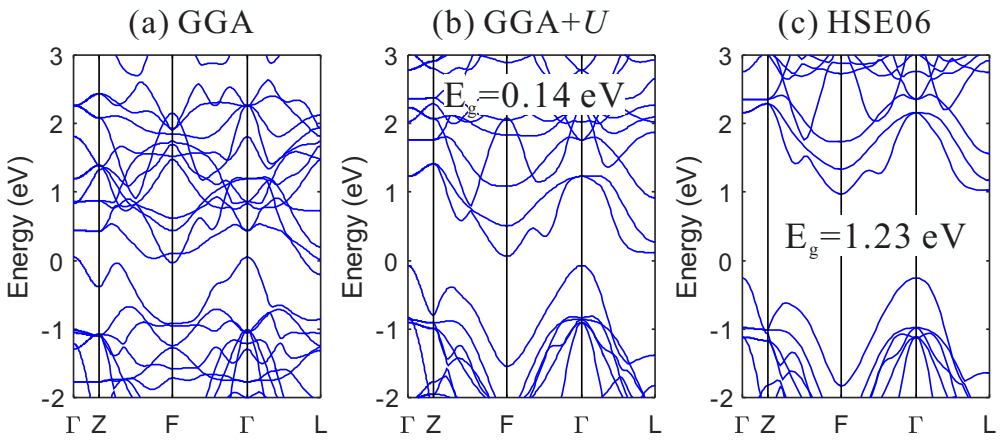

FIG. 7. Calculated energy band structures of FM γ-Cr_2S_3 bulk within (a) GGA, (b) GGA + U, and (c) HSE06 hybrid functional frameworks.

VBM of γ-Cr_2S_3 is mainly composed of Cr t_{2g} and S p states, while the CBM is dominated by Cr e_g and S p states.

H. Further discussion on γ-Cr_2S_3

As presented above, the vdW layered γ-Cr_2S_3 is an intrinsic FMI. One important feature is that its ferromagnetism is layer independent. Therefore, if obtaining FMIs from γ-Cr_2S_3, the sample can be as thin as one or several QLs, and it can also be as thick as a bulk. In this regard, the precise control of the film thickness becomes less important or unessential. On the other hand, the thickness control is still interesting to manipulate the energy gap. The thinner film has a larger energy gap, while the thicker film has a smaller gap. Thinner or thicker, the sample is always a FMI, but the energy gap is tuned from about 1.2 to 2.0 eV. This is quite different from CrI_3 and $Cr_2Ge_2Te_6$, whose magnetism is layer dependent [1,2]. The CrI_3 monolayer is FM. Its bilayer becomes AFM, while the trilayer returns to be FM again [2]. The $Cr_2Ge_2Te_6$ bilayer is a Heisenberg FMI, while in the monolayer limit the FM order is not present in experiment [1]. When obtaining FMIs from these two materials the film thickness must be carefully controlled, which is challenging in experiment. The Curie temperatures of γ-Cr_2S_3 were estimated using the mean-field approximation (MFA) [42]. Based on the HSE06 data, we got $T_C = 4$ and 38 K in 1QL and bulk cases, respectively. While using the GGA + U energies, the estimated temperatures increased to 14 and 88 K, respectively. The different Curie temperatures come from the energy difference within different calculations frameworks.

Though γ-Cr_2S_3 is a robust FMI against the film thickness, its magnetism as well as the energy gap can be manipu-

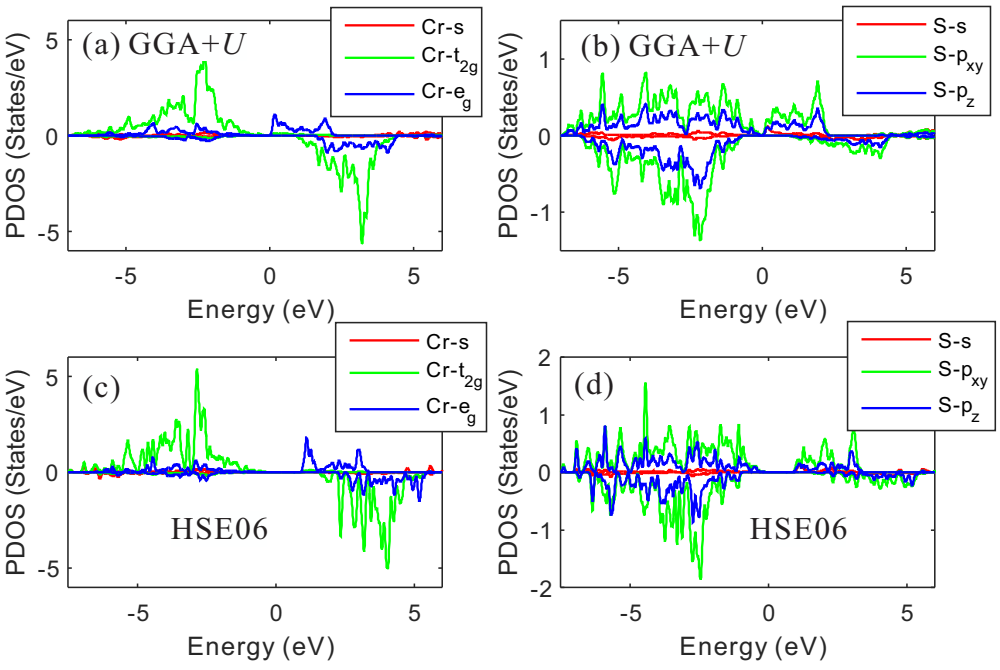

FIG. 8. Projected density of states of FM γ-Cr_2S_3 bulk within [(a), (b)] GGA + U and [(c), (d)] HSE06 frameworks.

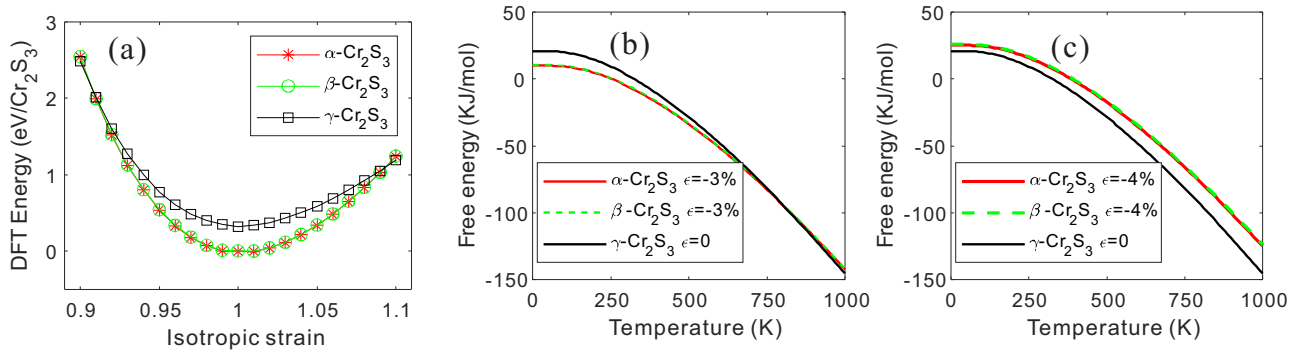

FIG. 9. (a) DFT (density functional theory) energy of α-, β-, and γ-Cr_2S_3 under isotropic strain. [(b), (c)] Free energy of the three phases of Cr_2S_3. The data were obtained based on the GGA + U (U = 3.0 eV) calculations.

lated by strains. The in-plane compressive strain facilitates the ferromagnetism and decreases the energy gap, while the in-plane tensile train does the opposite. In the 1QL case, an in-plane tensile strain of 0.5% turns γ-Cr_2S_3 from a FMI to an AFM insulator. Hence, the strain can be used not only as an energy-gap regulator besides the film thickness but also as a switch between FM and AFM insulators. Moreover, the in-plane lattice constant of γ-Cr_2S_3 is about 3.4 Å, which is approximately half of the lattice constants of CrI_3 and $Cr_2Ge_2Te_6$ monolayers [23,24]. This provides a new alternative when constructing heterostructures with other materials such as topological insulators from the point of lattice matching [7,43–45].

The most challenging task of γ-Cr_2S_3 may lie in the experimental realization. As discussed in Sec. III A, γ-Cr_2S_3 is about 0.14 eV/Cr higher in energy than α- and β-Cr_2S_3 within the GGA framework. For a better understanding of this energy difference, we examine the existing phases of other materials by taking Sb_2Te_3 as an example. In experiment, Sb_2Te_3 occurs at least in three phases, possessing the space groups of $C2/m$ (No. 12), $C2/c$ (No. 15), and R-3m (No. 166), respectively. For simplicity, we call the three phases of crystals according to their group numbers as 12-, 15-, and 166-Sb_2Te_3, respectively. Among them, 166-Sb_2Te_3 is a famous topological insulator and has the same crystal structure as γ-Cr_2S_3. Based on the GGA calculations, 166-Sb_2Te_3 has the lowest energy. 12-Sb_2Te_3 is 0.134 eV/Sb higher in energy than 166-Sb_2Te_3, very close to the energy difference of 0.14 eV/Cr in the Cr_2S_3 case. 15-Sb_2Te_3 is 0.309 eV/Sb higher in energy than 166-Sb_2Te_3, much higher than the 0.14 eV/Cr in the Cr_2S_3 case. Energetically, 12- and 15-Sb_2Te_3 crystals are metastable, while both of them were successfully synthesized in experiment. 12-Sb_2Te_3 was synthesized by quenching after high-pressure (4 GPa) and high-temperature (873 K) treatment [46]. 15-Sb_2Te_3 was realized under high pressure up to 9.8 GPa at room temperature [47]. Therefore, the energy difference of 0.14 eV/Cr is not an insurmountable energy barrier. Through controlling pressure or strain, temperature, and quenching process, γ-Cr_2S_3 is likely to be synthesized in experiment.

The energy difference between the γ phase and the other two phases of Cr_2S_3 decreases under strain. As Fig. 9(a) exhibits, the γ phase becomes energetically lower than the α and β phases at $\epsilon = \pm 10\%$. Yet, this strain is extremely large in experiment. Among the three phases of crystals, γ-Cr_2S_3 has the steepest-descent free energy following the temperature T. Even so, its free energy remains higher than that of α and β phases in the range T = 0–1000 K, which is adverse to the experimental synthesis of γ-Cr_2S_3. Strain can change the free-energy order of the three crystals. As Figs. 9(b) and 9(c) illustrate, compressing the lattice constants of α- and β-Cr_2S_3 by 3%, the free energy of γ-Cr_2S_3 becomes the lowest for $T \geqslant 800$ K. If the compression reaches 4% or larger, the free energy of the unstrained γ-Cr_2S_3 keeps the lowest at any temperature. The lattice constants of γ-Cr_2S_3 are very different from those of α- and β-Cr_2S_3. Hence, substrates having good lattice matching with γ-Cr_2S_3 usually cannot match the lattices of α- and β-Cr_2S_3 well. If the lattice mismatching reaches 3% or larger, α- and β-Cr_2S_3 are hard to be synthesized because of the higher free energy. On the contrary, in this situation the lowest free energy of γ-Cr_2S_3 renders it very likely to occur. Therefore, to grow γ-Cr_2S_3, hexagonal substrates with in-plane lattice constants around 3.4 Å are good candidates. Binary compounds such as ZrCl (869, 3.424), ScCl (1004, 3.473), $NiCl_2$ (14208, 3.483), Fe_3S_4 (42537, 3.470), ZrBr (1168, 3.503), $FeCl_2$ (4059, 3.598), Tl_2O (16220, 3.516), TiS (25561, 3.417), and Ti_2S_3 (86359, 3.440) meet this requirement well; thus, they are recommended. Here, the first number in the parentheses is the Inorganic Crystal Structure Database (ICSD) [48] collection code, while the second one is the in-plane lattice constant in angstroms.

IV. CONCLUSION

This work predicts a new structural phase of Cr_2S_3 (γ-Cr_2S_3) and further predicts that it is an intrinsic FMI. The crystal is vdW layered and dynamically metastable. Its in-plane lattice constant is around 3.4 Å, about half of the lattice constants of CrI_3 [23] and $Cr_2Ge_2Te_6$ [24]. The ferromagnetism of γ-Cr_2S_3 is rather robust and layer independent, which is confirmed by GGA, GGA + U, and HSE06 hybrid functional calculations. Bulk γ-Cr_2S_3 has indirect energy gap of 1.23 eV, which increases to 1.97 eV in the 1QL limit; thus, the gap value can be tuned between by changing the layer number or film thickness. The gap size and the magnetism can be controlled by in-plane strain. Compressive strain facilitates the ferromagnetism and decreases the energy gap of

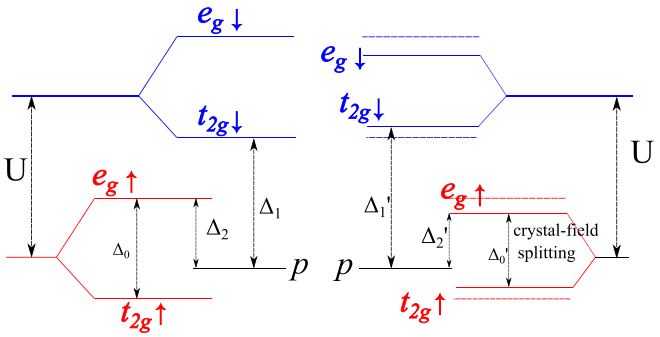

FIG. 10. The evolution of the energy levels after the tension is applied. The left panel is the configuration without strain and the right panel is that with tensile strain. The dashed lines in the right panel denote the energy levels before the strain is applied. The tension causes the enlargement of (CrS_6) units, which means the crystal-field splitting Δ_0 decreases. The unoccupied e_g orbitals get close to the Fermi level, leading to the decrease of the charge transfer energy Δ_2. On the contrary, the charge transfer energy Δ_1 increases.

1QL γ-Cr_2S_3, while tensile strain leads to antiferromagnetism and decreases the energy gap. About 0.5% tensile strain is enough to cause FM-AFM phase transition in 1QL γ-Cr_2S_3. Possessing the same crystal structure, γ-Cr_2Se_3 is an AFM insulator, but it can be turned into a FMI through moderate compressive strains. The experimental realization of γ-Cr_2S_3 is discussed and suggestions are proposed, and we call for experimental efforts.

ACKNOWLEDGMENTS

P.L. would like to thank F. F. Zhu for helpful discussions. This work was supported by the National Natural Science Foundation of China (Grant No. 11521404), the University Natural Science Research Project of Anhui Province (Grant No. KJ2020A0480), and the Natural Science Foundation of Anhui Province (Grant No. 2108085MB42).

APPENDIX

With various Cr-S bond length, the magnetic couplings of the Cr_2S_3 isostructures with regular (CrS_6) octahedrons evolves as shown in Fig. 10.

The detailed superexchange paths for J_2 and J_3 are schematically shown in Fig. 6. All angles of Cr-S-Cr which bridge the intermediate states of second-NN (third-NN) interlayer superexchange are nearly 90° (180°). We express the seven terms with subscripts according to the sequence in Fig. 6 as follows:

$$\begin{aligned}
\delta E_1 &\sim 16\left(\frac{t_{pd\pi}^2}{\Delta_1}\right)^2 \frac{J_H}{(2\Delta_1)^2},\\
\delta E_2 &\sim 8\left(\frac{t_{pd\pi}^2}{\Delta_1}\frac{t_{pd\sigma}^2}{\Delta_2}\right)\frac{3J_H}{(\Delta_1+\Delta_2)^2},\\
\delta E_3 &\sim -8\left(\frac{t_{pd\pi}^2}{\Delta_1}\right)^2 \frac{1}{2\Delta_1},\\
\delta E_4 &\sim -8\left(\frac{t_{pd\pi}^2}{\Delta_1}\frac{t_{pd\sigma}^2}{\Delta_2}\right)\frac{J_H}{(\Delta_1+\Delta_2)^2},\\
\delta E_5 &\sim -8\left(\frac{t_{pd\pi}^2}{\Delta_1}\right)^2 \frac{1}{2\Delta_1},\\
\delta E_6 &\sim -8\left(\frac{t_{pd\pi}^2}{\Delta_1}\frac{t_{pd\sigma}^2}{\Delta_2}\right)\frac{J_H}{(\Delta_1+\Delta_2)^2},\\
\delta E_7 &\sim 4\left(\frac{t_{pd\pi}^2}{\Delta_1}\right)^2 \frac{J_H}{(2\Delta_1)^2},
\end{aligned} \tag{A1}$$

where the positive sign means that FM coupling is favored and Hund's couplings of S and Cr are treated to be the same value for simplicity.

[1] C. Gong, L. Li, H. Ji, A. Stern, Y. Xia, T. Cao, W. Bao, C. Wang, Y. Wang, Z. Q. Qiu, R. J. Cava, S. G. Louie, J. Xia, and X. Zhang, Nature (London) **546**, 265 (2017).
[2] B. Huang, G. Clark, E. Navarro-Moratalla, D. R. Klein, R. Cheng, K. L. Seyler, D. Zhong, E. Schmidgall, M. A. McGuire, D. H. Cobden, W. Yao, D. Xiao, P. Jarillo-Herrero, and X. Xu, Nature (London) **546**, 270 (2017).
[3] Y. Guo, B. Wang, X. Zhang, S. Yuan, L. Ma, and J. Wang, InfoMat **2**, 639 (2020).
[4] K. S. Burch, D. Mandrus, and J.-G. Park, Nature (London) **563**, 47 (2018).
[5] A. H. MacDonald, P. Schiffer, and N. Samarth, Nat. Mater. **4**, 195 (2005).
[6] T. Dietl, Semicond. Sci. Technol. **17**, 377 (2002).
[7] P. Li, J. Yu, J. Xu, L. Zhang, and K. Huang, Phys. B: Condens. Matter **573**, 77 (2019).
[8] P. Li, J. Yu, Y. Wang, and W. Luo, Phys. Rev. B **103**, 155118 (2021).
[9] N. Samarth, Nature (London) **546**, 216 (2017).
[10] N. D. Mermin and H. Wagner, Phys. Rev. Lett. **17**, 1133 (1966).
[11] J. P. Perdew, K. Burke, and M. Ernzerhof, Phys. Rev. Lett. **77**, 3865 (1996).
[12] J. Heyd, G. Scuseria, and M. Ernzerhof, J. Chem. Phys. **118**, 8207 (2003).
[13] J. Heyd, G. Scuseria, and M. Ernzerhof, J. Chem. Phys. **124**, 219906 (2006).
[14] G. Kresse and J. Furthmüller, Phys. Rev. B **54**, 11169 (1996).
[15] J. Klimeš, D. R. Bowler, and A. Michaelides, J. Phys.: Condens. Matter **22**, 022201 (2010).
[16] C. P. Vicente, J. L. Tirado, K. Adouby, J. C. Jumas, A. A. Toure, and G. Kra, Inorg. Chem. **38**, 2131 (1999).
[17] X. Gonze and C. Lee, Phys. Rev. B **55**, 10355 (1997).
[18] K. Parlinski, Z. Q. Li, and Y. Kawazoe, Phys. Rev. Lett. **78**, 4063 (1997).
[19] A. Togo and I. Tanaka, Scr. Mater. **108**, 1 (2015).
[20] F. Jellinek, Acta Crystallogr. **10**, 620 (1957).
[21] E. F. Bertaut, J. Cohen, B. Lambert-Andron, and P. Mollard, J. Phys. France **29**, 813 (1968).

[22] B. Van Laar, Phys. Lett. A **25**, 27 (1967).
[23] W.-B. Zhang, Q. Qu, P. Zhu, and C.-H. Lam, J. Mater. Chem. C **3**, 12457 (2015).
[24] K. Wang, T. Hu, F. Jia, G. Zhao, Y. Liu, I. V. Solovyev, A. P. Pyatakov, A. K. Zvdzdin, and W. Ren, Appl. Phys. Lett. **114**, 092405 (2019).
[25] F. Cui, X. Zhao, J. Xu, B. Tang, Q. Shang, J. Shi, Y. Huan, J. Liao, Q. Chen, Y. Hou, Q. Zhang, and S. J. Pennycook, Adv. Mater. **32**, 1905896 (2020).
[26] J. Liu, Q. Sun, P. Kawazoe, and Y. Jena, Phys. Chem. Chem. Phys. **18**, 8777 (2016).
[27] H. Wang, V. Eyert, and U. Schwingenschlögl, J. Phys.: Condens. Matter **23**, 116003 (2011).
[28] Y. Zhang, W. Ding, Z. Chen, J. Guo, H. Pan, X. Li, Z. Zhao, Y. Liu, and W. Xie, J. Phys. Chem. C **125**, 8398 (2021).
[29] H. L. Feng, Z. Deng, C. U. Segre, M. Croft, S. H. Lapidus, C. E. Frank, Y. Shi, C. Jin, D. Walker, and M. Greenblatt, Inorg. Chem. **60**, 1241 (2021).
[30] D. Meng, H. Guo, Z. Cui, C. Ma, J. Zhao, J. Lu, H. Xu, Z. Wang, X. Hu, Z. Fu, R. Peng, J. Guo, X. Zhai, G. J. Brown, R. Knize, and Y. Lu, Proc. Natl. Acad. Sci. USA **115**, 2873 (2018).
[31] P. Li and W. Luo, Sci. Rep. **6**, 25423 (2016).
[32] D.-H. Kim, K. Kim, K.-T. Ko, J. H. Seo, J. S. Kim, T.-H. Jang, Y. Kim, J.-Y. Kim, S.-W. Cheong, and J.-H. Park, Phys. Rev. Lett. **122**, 207201 (2019).
[33] C. Zener, Phys. Rev. **82**, 403 (1951).
[34] T. Dietl, H. Ohno, and F. Matsukura, Phys. Rev. B **63**, 195205 (2001).
[35] J. B. Goodenough, *Magnetism and the Chemical Bond* (Interscience (Wiley), New York, 1963)
[36] D. I. Khomskii, in *Transition Metal Compounds* (Cambridge University Press, Cambridge, U.K., 2015), pp. 103–136.
[37] J. C. Slater and G. F. Koster, Phys. Rev. **94**, 1498 (1954).
[38] D. V. Eva Pavarini, E. Koch, and A. Lichtenstein, The LDA+DMFT approach to strongly correlated materials, Ph.D. thesis, German Research School for Simulation Sciences GmbH (2011).
[39] S. J. Duclos, Y. K. Vohra, and A. L. Ruoff, Phys. Rev. B **41**, 5372 (1990).
[40] M. Moreno, J. A. Aramburu, and M. T. Barriuso, Phys. Rev. B **56**, 14423 (1997).
[41] P. Li and W. Luo, Phys. Rev. B **94**, 075202 (2016).
[42] L. Seixas, A. Carvalho, and A. H. Castro Neto, Phys. Rev. B **91**, 155138 (2015).
[43] Y. Hao, Y. Gu, Y. Gu, E. Feng, H. Cao, S. Chi, H. Wu, and J. Zhao, Chin. Phys. Lett. **38**, 096101 (2021).
[44] D. Zhang, K. L. Seyler, X. Linpeng, R. Chang, N. Sivadas, B. Huang, E. Schmidgall, T. Taniguchi, K. Watanabe, M. A. McGuire, W. Yao, D. Xiao, K.-M. C. Fu, and X. Xu, Sci. Adv. **3**, e1603113 (2017).
[45] P. Li, Y.-W. You, K. Huang, and W. Luo, J. Phys.: Condens. Matter **33**, 465003 (2021).
[46] N. Serebryanaya, E. Tatyanin, S. Buga, I. Kruglov, N. Lvova, and V. Blank, Phys. Status Solidi B **252**, 267 (2015).
[47] S. M. Souza, C. M. Poffo, D. M. Trichês, J. C. de Lima, T. A. Grandi, A. Polian, and M. Gauthier, Phys. B: Condens. Matter **407**, 3781 (2012).
[48] R. Allmann and R. Hinek, Acta Crystallogr. A **63**, 412 (2007).